



A comprehensive kinetic framework for solid carbon deposition and hydrogen production from the pyrolysis of light hydrocarbons streams

Francesco Serse^a, Zhaobin Ding^{b,1}, Mauro Bracconi^b, Matteo Maestri^{b,*}, Andrea Nobili^a,
Clarissa Giudici^a, Alessio Frassoldati^a, Tiziano Faravelli^a, Alberto Cuoci^a, Matteo Pelucchi^{a,*}

^a CRECK Modeling Lab, Department of Chemistry, Materials and Chemical Engineering, Politecnico di Milano, Italy

^b Laboratory of Catalysis and Catalytic Processes, Department of Energy, Politecnico di Milano, Italy

ARTICLE INFO

Keywords:

Detailed kinetic modeling
Hydrocarbons cracking
Pyrocarbon deposition
Turquoise hydrogen
Density functional theory
Carbon materials
Soot

ABSTRACT

Thermal pyrolysis of hydrocarbons is a promising solution for the industrial production of hydrogen and valuable carbon materials. Pyrolysis reactor design and scale up strongly benefit from predictive chemical kinetic models capable to comprehensively describe the reactivity in the gas phase, including the undesirable formation of amorphous carbon (i.e., soot), as well as the solid carbon deposition mechanism. In this work, a methodology for the determination of rate constants of the heterogeneous growth of pyrocarbon deposit by means of theory-based corrections of analogous gas phase reactions is firstly proposed. Specifically, the theoretical methodology is applied to H-abstraction reactions governing the propagation of superficial active sites. Based on these findings, a detailed pyrocarbon deposition model from the literature is revised and coupled to a state-of-the-art model describing the dynamics of species evolution in the gas phase as well as the molecular growth of polycyclic aromatic hydrocarbons (PAHs) and soot. The model is validated with literature experimental data of pyrocarbon formation from light hydrocarbons feedstocks, covering a large set of operating conditions (pressure, temperature, surface over volume ratio). The comprehensive kinetic framework can reproduce the experimental deposition rates as well as the amount of deposited carbon with high fidelity under varying operative conditions. Moreover, kinetic analyses have been performed for assessing the relevant reaction pathways leading to pyrocarbon deposition from propane and methane feedstocks as well as the competition between carbon deposition and amorphous carbon formation.

1. Introduction

Thermal and thermocatalytic cracking of hydrocarbons is a promising solution for the production of hydrogen (H₂), a carbon neutral energy vector, and valuable carbon materials. This route is often referred to as “turquoise” and, compared to steam reforming (SR) currently covering > 95% of worldwide H₂ production (“gray” H₂), it allows to directly capture the carbon content in the form of materials, avoiding additional and costly separation steps such as CO₂ capture (“blue” H₂). The carbon product can be in the form of amorphous carbon (i.e., soot and carbon black) or in the form of structured carbon nanotubes, carbon fibers and graphene. Such possibility of producing materials in a single thermal or thermocatalytic process can potentially drive the price of H₂

to levels comparable to that of SR (i.e. 1–2 USD/kg [1,2]). Overall, while “green” H₂ from water electrolysis is being pursued as the main route to H₂ production from renewable energy sources, CO₂-free “turquoise” technologies enable a cleaner and sustainable exploitation of existing fossil sources, ultimately speeding up the energy transition [3]. This is particularly relevant for energy and CO₂ intensive production processes (e.g. metals, aluminum, steel industry) where “turquoise” H₂ accomplishes a remarkable materials-energy nexus. Indeed, together with the replacement of oil and natural gas with H₂ to satisfy the thermal power requirements of energy intensive industries, high performance, durable and recyclable carbon materials can potentially displace plastics and metals [4].

Abbreviations: SR, steam reforming; CVD, chemical vapor deposition; CVI, chemical vapor infiltration; BEP, Bell-Evans-Polanyi; BDE, bond dissociation energy; PAH, polycyclic aromatic hydrocarbon; TST, transition state theory; ZPVE, zero point vibrational energy; DSM, discrete sectional model; PSR, perfectly stirred reactor; PFR, plug flow reactor; HACA, hydrogen abstraction carbon addition; MAH, mono aromatic hydrocarbon; Z, zigzag; A, armchair.

* Corresponding authors.

E-mail addresses: matteo.maestri@polimi.it (M. Maestri), matteo.pelucchi@polimi.it (M. Pelucchi).

¹ Current affiliation: School of Chemical Engineering and Technology, Sun Yat-sen University, Zhuhai, 519082, China.

<https://doi.org/10.1016/j.cartre.2023.100263>

Received 10 February 2023; Received in revised form 7 April 2023; Accepted 14 April 2023

2667-0569/© 2023 The Author(s). Published by Elsevier Ltd. This is an open access article under the CC BY-NC-ND license

(<http://creativecommons.org/licenses/by-nc-nd/4.0/>)

During pyrolysis, hydrocarbon streams (C_xH_y) can be converted to H_2 and solid carbon (C_s) according to the global reaction



For instance, methane (CH_4) conversion to C_s and H_2 ($CH_4 \rightarrow C_s + 2H_2$) occurs through a well known radical chain mechanism [3]. Overall, this endothermic process requires an energy input of ~ 37.7 kJ to produce one mole of H_2 , which is lower than both water electrolysis (~ 285.8 kJ) and methane SR (~ 41.4 kJ, without considering water evaporation). Typically, non-catalytic and non-plasma activated endothermic cracking processes are operated at high temperatures ($T = 1000$ – 1500 K, depending on the feedstock) and low pressures ($P = 1$ – 50 kPa).

The investigation of pyrolytic carbon deposition mechanisms is not only of relevance in the context of a carbon neutral energy economy, but historically finds applications in many production processes of the chemical industry such as undesired coking phenomena in steam cracking units [5,6] or the production of carbon composites through chemical vapor deposition (CVD) and infiltration (CVI) processes [7]. Control over the texture of the deposit during growth is a key point in CVI and CVD as, depending on the degree of anisotropy, the final materials have different mechanical and optical properties [8]. This has been shown to strongly depend on process parameters such as temperature (T), pressure (P), residence time (τ) and surface-to-volume ratio (A/V). Moreover, as in the objectives of the present work, competition with soot formation in the gas phase should be also accounted for, highlighting the need of a comprehensive kinetic framework capable of describing in a detailed fashion the surface chemistry as well as the homogeneous gas phase chemistry. The chemical kinetics framework here proposed ultimately allows to identify optimal operating conditions to produce H_2 and graphitic carbon, as well as at describing its competition with undesired amorphous carbon particles (soot) formation in the gas phase. This work should be also considered propedeutical to the extension of CVD kinetic models to other hydrocarbon feedstocks and to the understanding of other non-catalytic and catalytic cracking processes of hydrocarbons producing, for example, carbon black or carbon-nanotubes.

Lacroix et al. [9] proposed a first detailed kinetic mechanism for pyrocarbon deposition which is based on similar reaction classes as those extensively applied to hydrocarbons pyrolysis and, specifically, in molecular growth kinetics leading to polycyclic aromatic hydrocarbons (PAHs) and soot formation [10]. H-abstractions, additions, β -scissions, ipso-additions, initiations and termination reactions occur both in the gas phase and on the solid surface. Rate parameters for gas-solid interactions were determined based on the analogy with gas phase prototype reactions involving benzene, with some modifications to account for reaction path degeneracy. Recent studies from Yonder et al. [11] and Ding et al. [12] support the validity of such approach.

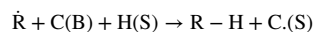
The surface mechanism proposed by Lacroix et al. [9] is coupled here with a comprehensively validated gas phase kinetic model for light hydrocarbons [13–15], including molecular growth kinetics to form PAHs as well as a recently upgraded soot formation model [16–18]. Following up on the first-principles assessment of Ding et al. [12], which has proven the existence of an empirical correlation between the energy barriers of H-abstraction reactions on methane, ethane and benzene in the gas phase with those on a graphene monolayer based on PBE-D2 density functional theory calculations, a theoretical methodology for the determination of rate constants for pyrocarbon deposition applications is presented. This allows the definition of semi-empirical corrections applicable to better estimate rate constants of gas phase reactions and thus to derive more reliable model parameters for the heterogeneous carbon deposition and growth process. The rate constants of H-abstraction reactions at the gas-solid interface so determined, both for armchair and zigzag sites, are used to update the model from Lacroix et al. [9]. The updated model is validated on literature data measuring both species formation in the gas phase and pyrocarbon deposition rates. Kinetic analyses are used to identify major reaction pathways and to unravel

the competition between deposition and soot formation processes and its dependence on operating conditions.

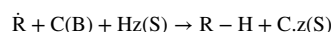
2. Kinetic model for CVD

The solid carbon deposition mechanism of Lacroix et al. [9] involves 275 reactions and 66 surface species. 131 elementary steps describe the reactivity of armchair sites, whereas the remaining 144 describe zigzag sites. The overall structure of the solid carbon deposition model from Lacroix et al. [9] is reiterated in Section S1 of the Supplementary Material (SM) reporting some of the most relevant heterogeneous reaction pathways (Figure S1–Figure S8). Surface reactivity is initiated through H-abstraction reactions by gas phase radicals (e.g., \dot{H} , $\dot{C}H_3$, C_3H_5 -A, $CH_2\dot{C}H$).

The generic H-abstraction reaction can be written as



and



for armchair (C.(S)) and zigzag sites (C.z(S)), respectively. Once the surface sites are activated, addition to molecules or recombination with radicals in the gas phase can occur to eventually yield an additional aromatic structure. Rate constants for H-abstraction reactions are updated based on the theoretical analysis presented in Section 3 of this work. For the sake of completeness, a further modification has been introduced to account for the deposition of benzyl radical (C_7H_7) as a key intermediate for larger aromatics growth at high temperatures [17]. Its deposition mechanism (Fig. 1) on zigzag sites has been introduced in analogy with phenyl radical (Figure S6), where C_7H_7 binds to the solid surface by means of recombination with a superficial active site C.z(S) forming $C_7H_7(S)$. This superficial species can be activated for further propagation by H-abstraction from mostly \dot{H} or $\dot{C}H_3$ radicals leading to the $C_7H_6(S)$ species. Finally, six carbon bulk C(B) atoms and four H(S) are formed with a cyclization reaction together with one $CH_2Bz(S)$ species whose consumption leading to growth of carbon bulk is detailed in Figure S9 of the SM.

3. Rate constants determination

The evaluation of kinetic constants of H-abstraction reactions on gas phase prototype compounds by \dot{H} , $\dot{C}H_3$ and higher molecular weight alkyl and alkenyl radicals ($CH_2\dot{C}H$, $CH_3\dot{C}H_2$, $CH_3\dot{C}CH_2$, $\dot{C}H_2CHCH_2$, $\dot{C}H_2CH_2CH_3$, $(CH_3)_3\dot{C}$ and $n\dot{C}_4H_7$) has been performed with canonical TST. The potential energy surface, harmonic vibrational frequencies as well as hindered rotors potential have been calculated with the M062X functional [19]. This functional has been selected because of its recognized superior efficiency for describing non covalent $\pi \cdots \pi$ stacking interactions [20], which are relevant for determining transition states of H-abstractions on aromatic compounds by unsaturated radical species. Calculations with complete basis set (CBS) methodologies [21,22] have also been performed supporting the validity of the findings at the M062X level. Additional details on the adopted methodology are reported in the SM (Sections S2–S4). In particular, a preliminary benchmark validation of the accuracy of the adopted methods is performed by comparing calculated bond dissociation energies (BDEs) for gas phase prototype molecules of the abstracting radicals to values from the Active Thermochemical Tables Database [23] in Table S1. Mean unsigned errors in the range of 1.1 to 1.8 kcal/mol are obtained for CBS-QB3 [21,22] and M062X, respectively. The hindered rotor partition functions calculated using EStokTP [24] are reported in the Section S3 of SM together with a more specific description of entropic corrections to the rate constants given from the hindered rotors treatment.

As a first step, rate constants for H-abstractions on benzene by \dot{H} , $\dot{C}H_3$, $CH_2\dot{C}H$ (\dot{C}_2H_3), $CH_3\dot{C}H_2$ (\dot{C}_2H_5) are calculated in the temperature range 500–2000 K and compared with gas-phase experimental and

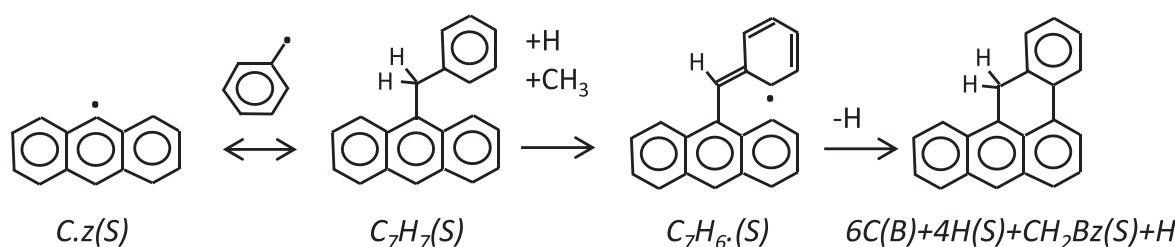


Fig. 1. Mechanism of benzyl radical deposition on zigzag sites.

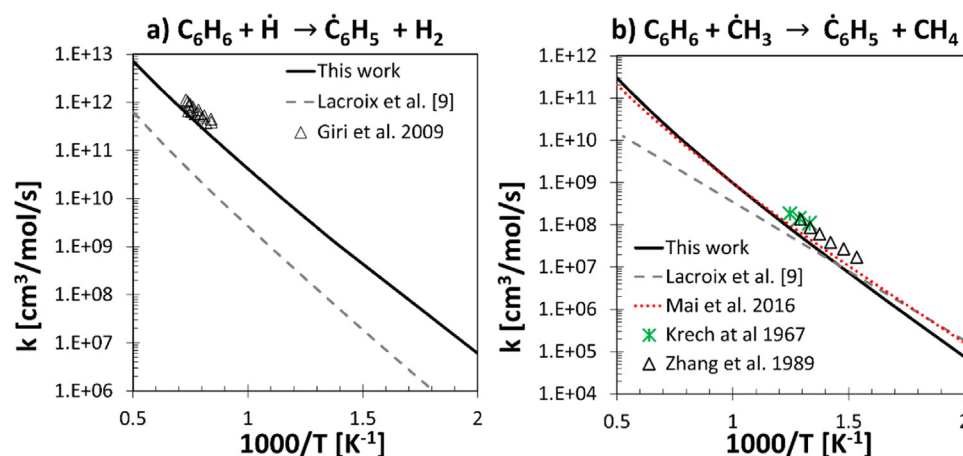


Fig. 2. Comparison between the available experimental data (symbols) [25–28] and results from theoretical calculations from this work (solid lines) for H-abstraction rate constants by \dot{H} (a), \dot{CH}_3 (b). Values from Lacroix et al. [9] are also reported for comparison (dashed lines).

theoretical data from the literature in Fig. 2, proving the reliability of the theoretical protocol for homogeneous rate constants. For the sake of brevity, only H-abstractions by \dot{H} and \dot{CH}_3 in the forward direction are reported. Additional comparisons for backward reactions and for H-abstractions by other radicals are shown in Figure S13 of the SM.

Fig. 2a reports the abstraction by H atom to form H_2 and phenyl radical (\dot{C}_6H_5). Calculations agree with experimental data [25–28] within a factor of ~ 2 in both directions (Figure S13a). The rate constant from Lacroix et al. [9] deviates by about an order of magnitude for $C_6H_6 + H \rightarrow \dot{C}_6H_5 + H_2$, showing instead a good agreement in the backward direction. This result suggests that the thermodynamic equilibrium of the hydrogen abstraction by \dot{H} in [9] deviates from the experimental evidence. Fig. 2b shows the rate constants for the H-abstraction by methyl radical (\dot{CH}_3) on benzene. Once again our values agree within a factor < 2 with the measurements. By looking at the temperature range for which the experimental data is available, namely from 1180 K to 1370 K, the rate constant found in the model of Lacroix et al. [9] shows on average the same deviation from the experiments as our computational predictions. Our results are also in agreement with the theoretical results of Mai et al. [28], which were obtained at a higher level of theory. However, at temperatures below those typical of pyrocarbon deposition process ($T < 1200$ K) the calculations from Mai et al. [28] are more similar to the rate provided by Lacroix et al. [9].

3.1. Derivation of Bell-Evans-Polanyi correlations for H-abstraction reactions

Energy barriers of H-abstraction reactions have been calculated for gas phase prototype polycyclic aromatic hydrocarbons (PAHs), ranging from one ring (benzene) to four rings (tetracene) so as to unravel possible size effects. The existence of a Bell-Evans-Polanyi (BEP) linear relationship [29] between the forward energy barriers and the C–H bond energy (Tables S1 and S2 in the SM) of the abstracting radicals is highlighted in Fig. 3a for the three different theoretical methods adopted and considering benzene as the model molecule. The results show that the M062X systematically underestimates energy barriers of activation

as well as BDEs of the abstracting radicals. Nevertheless, the slope of the BEP correlation is not affected by the level of theory. Moreover, reported results are in notable agreement, in terms of slope and intercept, with respect to the previous work by Ding et al. [12] with PBE-D2, therefore the results from M062X model have been considered valid. The BEP plot in Fig. 3b shows energy barrier for H-abstractions on tetracene, anthracene, phenanthrene (zigzag and armchair) proving the size independency of the correlations and endorsing benzene as an appropriate prototype compound for the theoretical evaluation of microkinetic parameters of heterogeneous pyrocarbon deposition mechanism.

3.2. Correlation between gas phase and graphene edges

Once the existence of BEP relationships has been proven for purely gas phase and gas/solid H-abstractions [12], the two linear trends can be exploited to directly derive a linear correlation between the energy barriers of homogeneous and heterogeneous H-abstractions. Fig. 4 shows the results for the PAHs here investigated.

The energy barriers of H-abstractions on zigzag and armchair sites are well correlated with the corresponding energy barriers found in homogeneous gas phase, with determination coefficients (R^2) equal to 0.958 and 0.970, respectively. The different trends found for armchair and zigzag sites highlight the different reactivities of the two edges of the graphitic surface. In particular, the energy barriers of H-abstractions on armchair sites are generally higher than the ones on zigzag sites, meaning that H-abstractions from zigzag sites are favoured. This is also true from an entropy change point of view. In fact, the corrections derived from the study of hindered rotors in the transition state (Section S3 of SM) leads to higher rate constants for the abstractions on zigzag sites with respect to the ones of armchair sites. Overall, the empirical correlations obtained with the M062X functional allow to derive energy barriers of heterogeneous gas/solid reactions from those of prototype molecules in homogeneous gas phase, for which more consolidated theoretical approaches exist [30].

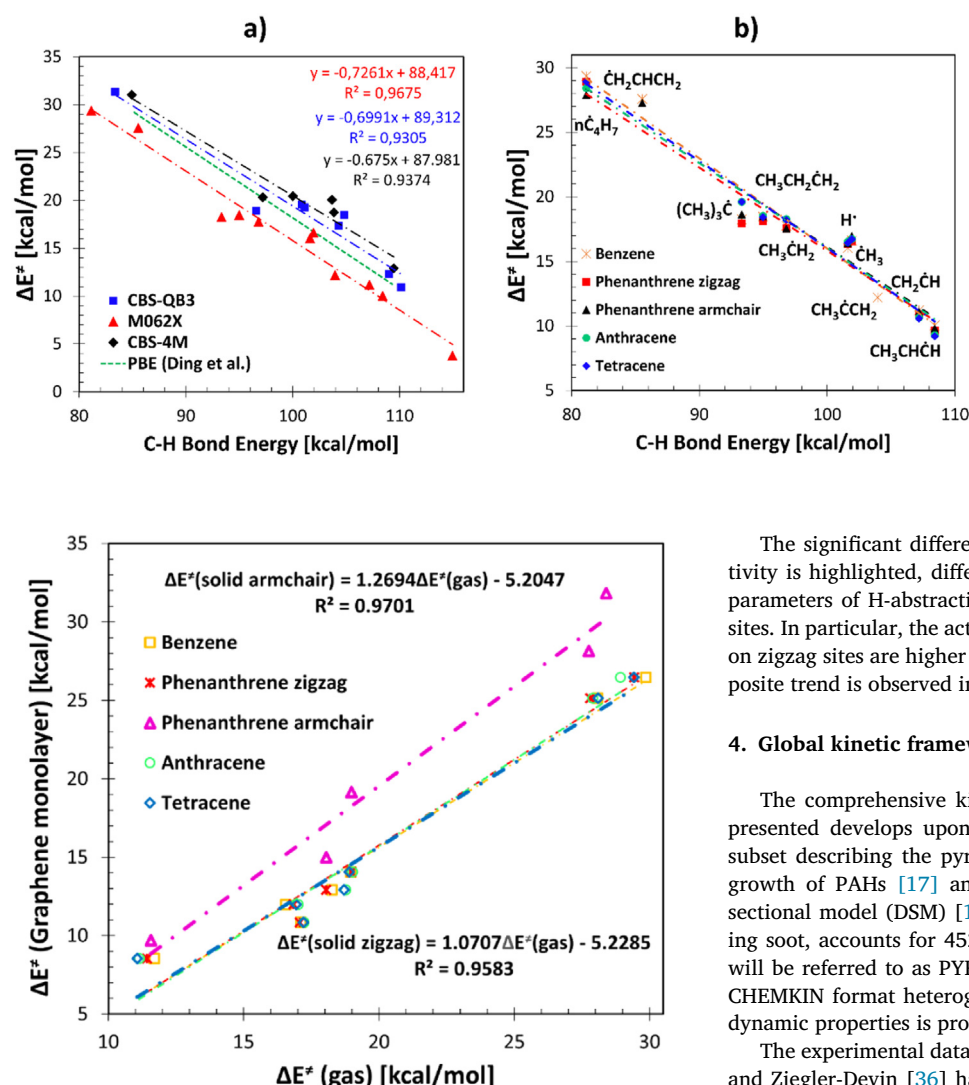


Fig. 4. correlation between homogeneous gas phase and heterogeneous gas-solid energy barriers of H-abstraction reactions obtained at the M062X/6-311+G(d,p) and PBE-D2 levels of theory, respectively. The heterogeneous gas-solid energies have been obtained for H-abstractions on a graphene monolayer with periodic calculations [112].

3.3. Heterogeneous rate constants determination

Starting from the analogy between elementary steps in gas and gas/solid environments explored empirically by Lacroix et al. [9], reaction rate constants are here derived by means of a TST based methodology. Indeed, it is possible to correct homogeneous gas phase rate constants to account for surface effects and for the different reactivities of armchair and zigzag sites. Therefore, the validated gas phase rate constants found for H-abstractions on benzene (Fig. 2) have been corrected, on one side, by modifying the potential energy barrier with the empirical correlations between gas phase and gas/solid energy barriers (Section 3.2, Fig. 4) and on the other side by adding the configurational correction discussed in Section S3 of the SM. Arrhenius parameters for forward and backward rate constants evaluated according to the present workflow are provided in Table S4 of the SM and they have been implemented in the modified version of Lacroix et al. [9] mechanism.

As an example, Fig. 5 reports the forward rate constants of H-abstraction by $\dot{\text{H}}$ (Fig. 5a) and $\dot{\text{CH}}_3$ (Fig. 5b) on zigzag and armchair sites compared with the reference gas phase reaction rates on benzene (Fig. 2) and the rate parameters proposed by Lacroix et al. [9].

Fig. 3. Linear relationship between forward energy barriers of H-abstraction reactions and the C-H bond dissociation energy of the abstracting radical. These energies are calculated with M062X/6-311+G(d,p) on a set of gas phase PAHs.

The significant difference between zigzag and armchair sites reactivity is highlighted, differently from Lacroix et al. [9], where kinetic parameters of H-abstractions were assumed equal for the two surface sites. In particular, the activation energy of H-abstraction by $\dot{\text{H}}$ and $\dot{\text{CH}}_3$ on zigzag sites are higher than those on armchair sites, whereas the opposite trend is observed in the backward direction.

4. Global kinetic framework and reactor models

The comprehensive kinetic model for pyrocarbon deposition here presented develops upon an extensively validated gas phase kinetic subset describing the pyrolysis of C1-C16 hydrocarbons [31–33], the growth of PAHs [17] and the formation of soot through a discrete sectional model (DSM) [16,18]. Overall, the gas phase subset, including soot, accounts for 452 chemical species and 24,041 reactions and will be referred to as PYR-SOOT model in the following sections. The CHEMKIN format heterogeneous kinetic model together with thermodynamic properties is provided in the SM.

The experimental datasets of Lacroix et al. [9], Ziegler et al. [34,35] and Ziegler-Devin [36] have been reproduced with an isothermal and isobaric heterogeneous perfectly stirred reactor (PSR), whereas a heterogeneous plug flow reactor (PFR) has been used to simulate the data of Brüggert et al. [37]. A brief overview of the governing equations for the two reactors and simulation details are given in the SM (Section S7) together with a summary of the validation conditions [9,34–37] (Section S8, Table S5). The solution of ideal reactors for model validation is carried out using OpenSMOKE++ [38].

All simulations are carried out considering the presence of a carbon preform whose composition has been assumed to be 50% zigzag and 50% armchair sites at the initial time of the deposition process coherently with the assumption of Lacroix et al. [9]. This is justified by the fact that the surface mechanism was insensitive to changes in the zigzag to armchair ratio. Parametric analyses on the relative amounts of zigzag and armchair surface sites have also been performed in this study, confirming the assumption of Lacroix et al. [9].

5. Results and kinetic analysis

The revised model here proposed is validated by comparison with different experimental datasets (Table S5). Datasets from [9,34–36] measure propane pyrolysis in a perfectly stirred reactor under varying operating conditions. Experimental measurements from [37,39] investigate pyrocarbon deposition from a CH_4 /argon mixture in a hot wall flow reactor. In the case of propane pyrolysis, experiments are carried out at a total pressure $P = 2.6$ kPa in nitrogen with a propane/nitrogen ratio of 1/9. Parametric analyses are conducted on temperature ($T = 1173$ – 1323 K), residence times ($\tau = 0.5$ – 4 s) and on the ratio between the pre-

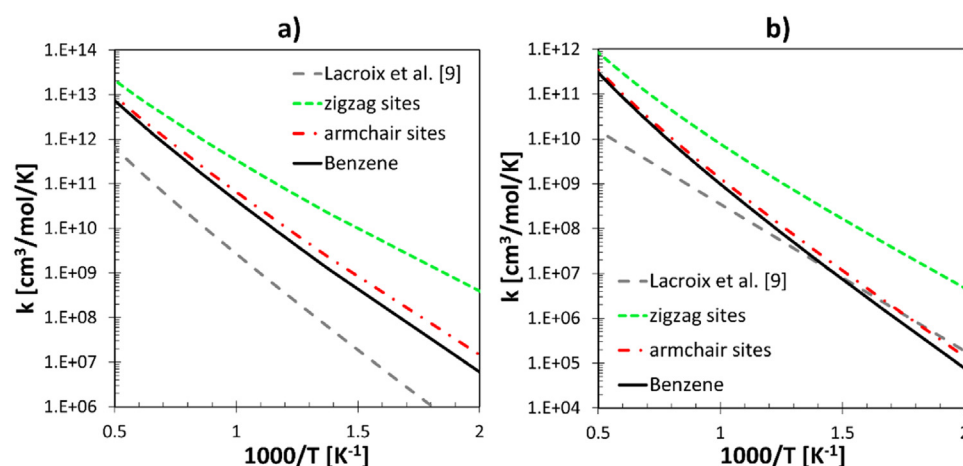


Fig. 5. Corrected rate constants of H-abstraction reactions accounting for the different reactivity of armchair and zigzag edges of graphene. a) rate parameters for the H-abstractions by $\dot{\text{H}}$; b) rate parameters for the H-abstraction by $\dot{\text{CH}}_3$. The corrected rate constants are compared with those in the mechanism of Lacroix et al. [9] (gray dashed line) and with the respective gas phase rate constants (solid black line).

form surface area and reactor volume (i.e., A/V) keeping T , τ and deposition time (or reaction time, t_R) constant. In the case of CH_4 pyrolysis [37,39], experiments are carried out in a flow reactor over a narrow temperature range ($T = 1323\text{--}1398\text{ K}$), at $P = 10\text{--}100\text{ kPa}$ and residence times of $0.2\text{--}1\text{ s}$.

The above studies characterize both species evolution in the gas phase with gas chromatography as well as the formation of deposited carbon. Data about the mass of deposited carbon is provided by directly weighting the preform before and after the deposition. Extensive comparisons and a thorough discussion related to gas phase species formation are reported in Section S9 of the SM. The deposition experiments are carried out both with and without a carbon preform.

For sake of brevity, the discussion in the next section mostly focuses on the effect of residence times, temperature, H_2 addition and A/V ratio on pyrocarbon deposition rates, mass, and on the competition with soot formation in the homogeneous phase. Beyond improved agreement with measured deposition rates and mass, this analysis aims at underlining the need of rigorously accounting for PAHs growth and soot formation when modeling pyrocarbon deposition processes. Moreover, the improved agreement proves the applicability of the proposed kinetic framework for optimal reactor design (e.g. to minimize the formation of unwanted amorphous carbon in the gas phase) or experimental interpretation purposes.

Concerning gas phase intermediates, a similar degree of accuracy (i.e. agreement well within a factor of 1.5) is generally observed when comparing our model to the experimental measurements and predictions from Lacroix et al. model [9] for key intermediates species such as H_2 , CH_4 , C_2H_2 , C_2H_4 , C_3H_6 and C_3H_4 . Differences in performance mainly result from the different underlying gas phase subset and from different rate constants for H-abstractions by key gas phase radicals (i.e. $\dot{\text{H}}$ and $\dot{\text{CH}}_3$) on surface sites (Fig. 5). More significant deviations are observed for monoaromatic (e.g. benzene, styrene, phenylacetylene) and polycyclic aromatic (e.g. naphthalene, C_{10}H_8) compounds. This is justified by a higher degree of detail used to describe PAHs growth [16] and by the inclusion of a soot formation subset [18].

5.1. Residence time effect

Fig. 6 compares deposition rate data and model from Lacroix et al. [9] with results from the present model at $T = 1273\text{ K}$, $P = 2.6\text{ kPa}$ and $\tau = 0.5\text{--}4\text{ s}$. The present model better predicts the measured deposition rate, especially at low residence times, whereas at higher residence times the performances of the two models are comparable and in agreement with experiments.

Accounting for soot formation is conducive to the observed decrease in deposition rate with respect to [9], allowing to better match qualitatively and quantitatively the experiments. The mass fraction of amor-

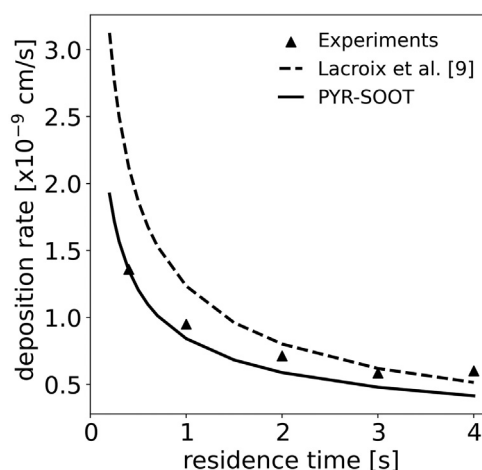


Fig. 6. Comparison of the models with experimental data [9] for the deposition rate [cm/s] at different residence times in the PSR. $T = 1273\text{ K}$, $P = 2.7\text{ kPa}$, $t_R = 90\text{ min}$, $A/V = 44\text{ cm}^{-1}$.

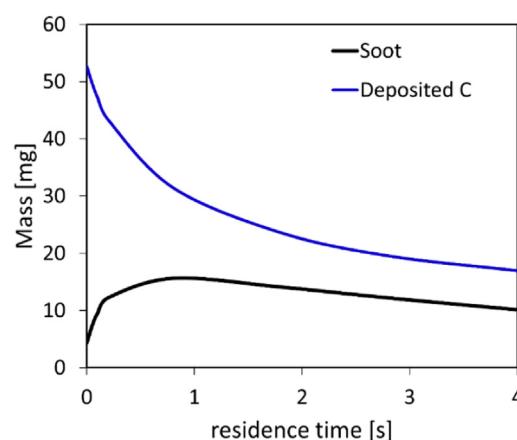


Fig. 7. comparison between mass of amorphous carbon and deposited carbon as a function of residence time in the reactor. Results have been obtained in a PSR after $t_R = 90\text{ min}$ with $T = 1273\text{ K}$, $A/V = 44\text{ cm}^{-1}$ and $P = 2.7\text{ kPa}$.

phous carbon (soot) can be obtained by summing all the carbon particles ranging from 320 to $3 \cdot 10^8$ carbon atoms [16–18].

Fig. 7 reports a parametric analysis on residence time of the surface perfectly stirred reactor, comparing the mass of deposited carbon

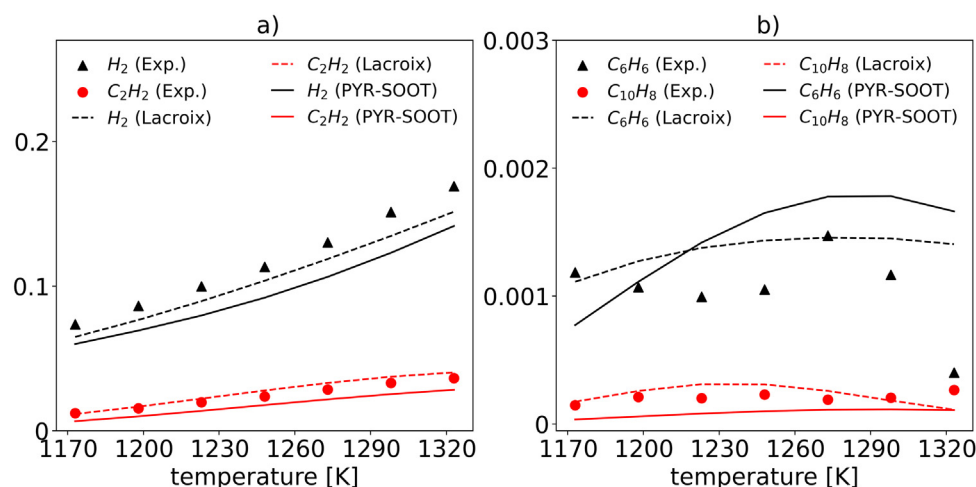


Fig. 8. Comparison of molar fraction profiles with experimental data [9] for hydrogen (H_2) (a), acetylene (C_2H_2) (a), benzene (C_6H_6) (b) and naphthalene ($C_{10}H_8$) (b) at different reactor temperatures. $t_R=90$ min, $\tau=1$ s, $A/V = 44$ cm $^{-1}$, $P = 2.7$ kPa. Dashed lines correspond to the original model of Lacroix et al. [9], solid lines correspond to the revised model from the present work.

(blue line) with that of amorphous carbon (black line) formed after $t_R = 90$ min at $T = 1273$ K and $A/V = 44$ cm $^{-1}$, which is calculated as in Eq. (1).

$$m_{soot} = \frac{V}{\tau} \frac{PMW^{in}}{RT} \omega_{soot} t_R \quad (1)$$

The overall mass flowrate entering the reactor is calculated by multiplying the volumetric flowrate, which is the ratio between the reactor volume (V) and the residence time (τ) inside the PSR, times the overall gas density (kg/m 3) in the ideal gas approximation (PMW^{in}/RT). Then, soot mass flowrate is obtained by multiplying the overall mass flowrate by the mass fraction of soot (ω_{soot}). Finally, the soot mass is obtained by multiplying the mass flowrate times the reaction time (hours) in the PSR (t_R). As discussed previously [16,18], the discrete sectional soot model treats particles as gas phase pseudo-species. Results show that soot mass initially increases up to a residence time of 1 s, where it reaches a maximum, then monotonically decreases. Deposited carbon mass, instead, monotonically decreases for increasing residence times. This is justified by the fact that, at higher residence times (τ) (i.e., lower mass flowrate at the reactor inlet if the volume is kept fixed) the deposition surface is exposed to a progressively lower quantity of carbonaceous precursors thus decreasing the deposition rate inside the reactor (Fig. 6). The same observation is valid for the results in Fig. 7 where both the masses of deposited and amorphous carbon decrease at longer residence times.

5.2. Temperature effect

Fig. 8 and Fig. 9 compare results from our model with experimental data and with the original model [9]. The present model underestimates the experimental H_2 profile, but correctly captures its increasing trend with temperature. A slightly better prediction is achieved by the original model of Lacroix et al. [9]. Acetylene (C_2H_2) is underestimated by a factor < 1.5 while benzene prediction is qualitatively in good agreement with the experimental trend, reaching a maximum at around 1280 K when it starts decreasing due to molecular growth to PAHs as also represented by increasing $C_{10}H_8$ yields.

Predicted carbon deposition rate [cm/s] is a factor of ~ 1.25 lower compared to the model of Lacroix et al. [9] and in excellent agreement with the experiments. As temperature increases, deposition reactions of gaseous species with increasing molecular weight (i.e. $> C_3$) are progressively activated, yielding a higher deposition rate.

Fig. 10 shows the competition between amorphous carbon and deposited carbon at $T = 1173$ – 1600 K, $\tau = 1$ s, $t_R = 90$ min, $A/V = 10$ cm $^{-1}$ (dashed line) and 44 cm $^{-1}$ (solid line). The present model predicts that the heterogeneous deposition of pyrocarbon becomes dominant for increasing temperatures. In fact, soot mass displays a maximum at relatively low temperatures whereas the mass of deposit steadily grows

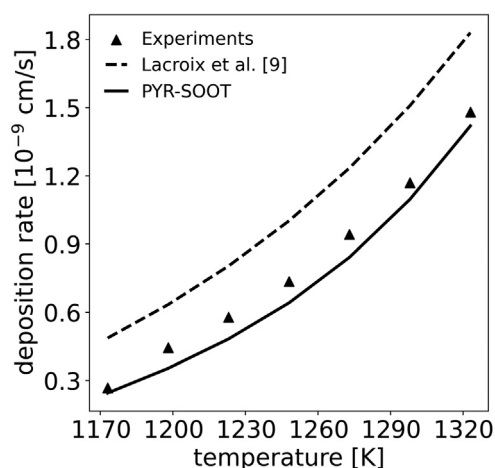


Fig. 9. Comparison of the models with experimental data [9] for the deposition rate [cm/s] at different reactor temperatures in the PSR. $P = 2.7$ kPa, $\tau=1$ s, $t_R=90$ min.

at increasing temperatures. The trend of amorphous carbon mass can be explained by considering that the density of the gaseous mixture (PMW^{in}/RT , see eq. (1)) decreases as temperature increases resulting in a lower overall mass flowrate entering the reactor. By contrast, soot mass fraction (ω_{soot}) monotonically increases with temperature. As a result, when the two opposing trends are balanced a null slope is observed. Furthermore, by comparing the solid lines ($A/V = 44$ cm $^{-1}$) with the dashed lines ($A/V = 10$ cm $^{-1}$), it stands out that low A/V ratios enhance amorphous carbon formation with respect to deposited carbon, as expected. Specifically, the higher the temperature the lower the amount of amorphous carbon and the higher the solid carbon deposited.

A rate of production analysis [38] on carbon bulk has been performed at the lowest ($T = 1173$ K) and highest ($T = 1323$ K) experimental temperatures (Fig. 11). Red bars indicate a negative contribution to the production of carbon bulk C(B), which means that the solid carbon is consumed, while blue lines indicate a positive contribution to the carbon deposit. The solid carbon rates of production and consumption are expressed in terms of kilograms per unit volume of the reactor (i.e., kg/m 3), which is integrated over the whole deposition time.

At the lower temperature condition (Fig. 11a) the surface carbon C(B) is mainly consumed by H-abstraction by \dot{H} and \dot{CH}_3 to produce armchair active sites (C.(S)). A more limited role is highlighted for H-abstractions by the same radicals yielding zigzag sites (C.z(S)). Deposition of ethylene (C_2H_4) on armchair sites triggers the reaction path-

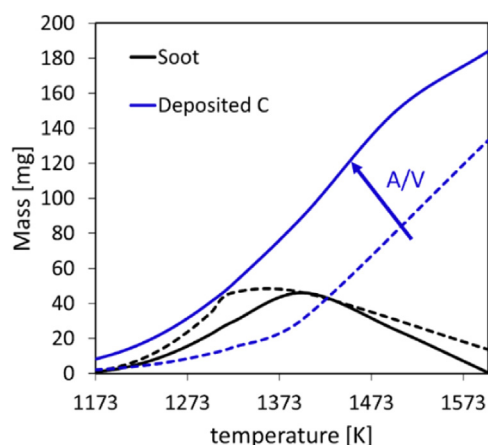
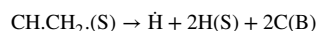
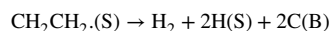


Fig. 10. Amorphous carbon (soot) mass (black lines) and deposited carbon mass (blue lines) [mg] as a function of the operating temperature at constant $A/V = 44 \text{ cm}^{-1}$ (continuous line) and $A/V = 10 \text{ cm}^{-1}$ (dashed line), $P = 2.7 \text{ kPa}$, $\tau = 1 \text{ s}$, $t_R = 90 \text{ min}$.

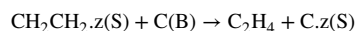
way reported in Figure S1 of the SM producing the surface species $\text{CH}_2\text{CH}_2(\text{S})$ that undergoes internal addition (i.e. cyclization) eliminating a surface hydrogen atom through β -scission. The stable surface species thus obtained ($\text{CH}_2\text{CH}_2(\text{S})$) undergoes H-abstraction or homolytic C–H fission forming $\text{CH}_2\text{CH}_2(\text{S})$. This latter species undergoes β -scission releasing a hydrogen atom $\dot{\text{H}}$ in the gas phase and two carbon bulk atoms $\text{C}(\text{B})$



Four-center molecular decomposition of $\text{CH}_2\text{CH}_2(\text{S})$ through the following reaction contributes to a lower extent to surface growth.



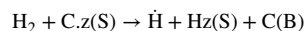
Deposition of C_2H_4 on zigzag sites is overall less effective, despite the higher rate constants for H-abstractions compared to armchair (Fig. 5), as the surface radical species $\text{CH}_2\text{CH}_2.z(\text{S})$ undergoes backward dissociation to produce ethylene and a $\text{C}.z(\text{S})$.



In its current form the updated Lacroix et al. [9] model requires deposition of C_2 species for effective growth from armchair sites and of C_3 species for growth from zigzag sites. Deposition of C_2 species on zigzag sites would indeed lead to the formation of 5-membered aromatic structures causing texture defects, whereas a 6-membered ring requires the combination of $\text{C}_1 + \text{C}_2$ species which in our study has a negligible contribution to the final mass of deposit. Future extensions of the present model will also take into account the formation of defects paving the way toward a more comprehensive understanding of pyrocarbon growth

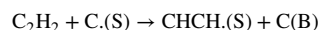
dynamics and of its quality. Overall, the dominant role of ethylene is consistent with the well-known steps of propane (C_3H_8) pyrolysis where H-abstractions from the primary carbon yields n-propyl radical ($\dot{\text{C}}_3\text{H}_7$) that decomposes through β -scission forming C_2H_4 and $\dot{\text{C}}\text{H}_3$.

Reverse H-abstraction by active sites $\text{C}.z(\text{S})$ transforming H_2 in reactive $\dot{\text{H}}$ atoms also contributes to $\text{C}(\text{B})$ formation.

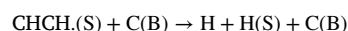


A limited role to $\text{C}(\text{B})$ formation is also played by deposition of vinylacetylene (C_4H_4). C_4H_4 is produced in the gas phase by methyl radical addition to allene ($\text{C}_3\text{H}_4\text{-A}$) or propyne ($\text{C}_3\text{H}_4\text{-P}$) followed by $\dot{\text{H}}$ elimination, or by recombination with propargyl radical ($\dot{\text{C}}_3\text{H}_3$) to form butadiene (C_4H_6) which undergoes H-abstraction and dehydrogenation by β -scission. Allene and propyne are formed by successive reactions of propene (C_3H_6) originating from H-abstractions from the secondary carbon site of propane followed by H-elimination through β -scission ($\text{CH}_3\dot{\text{C}}\text{HCH}_3 = \text{H} + \text{C}_3\text{H}_6$). Then, H-abstraction from C_3H_6 predominantly form resonance stabilized allyl radical ($\dot{\text{C}}_3\text{H}_5\text{-A}$) that decomposes to propyne or allene via β -scission ($\text{A-C}_3\text{H}_5 = \text{P-C}_3\text{H}_4/\text{A-C}_3\text{H}_4 + \text{H}$).

As expected from the higher temperature conditions at $T = 1323 \text{ K}$ the deposition of C_2H_2 (Figure S2) and $\dot{\text{C}}_6\text{H}_5$ (Figure S6) become more relevant and, together with the cyclization and the four-center molecular reactions on armchair sites coming from ethylene deposition discussed above, have the highest individual positive contributions to carbon deposition. In particular acetylene deposits on the surface armchair sites forming the surface radical species $\text{CHCH}(\text{S})$ through the reaction



$\text{CHCH}(\text{S})$ then undergoes cyclization eliminating a surface hydrogen atom through β -scission via



Backward H-abstraction by surface armchair radicals on H_2 and CH_4 restoring $\dot{\text{H}}$ and $\dot{\text{C}}\text{H}_3$ in the gas phase also contributes significantly to $\text{C}(\text{B})$ growth. H-abstraction by $\dot{\text{H}}$ on armchair sites dominates $\text{C}(\text{B})$ consumption, together with lower contributions of H-abstractions by $\dot{\text{C}}\text{H}_3$ on armchair sites and H-abstractions by $\dot{\text{H}}$ on zigzag sites.

Fig. 12 summarizes the contributions of the different reaction classes to the formation/consumption of $\text{C}(\text{B})$, confirming the increasing relative contribution of acetylene deposition for increasing temperature and the relevant role of C_2H_4 deposition over the entire temperature range. Overall, H-abstraction on armchair sites are the most influential reactions for the propagation of the solid carbon growth mechanism throughout the temperature range of validation. H-abstractions on zigzag sites, specifically by $\dot{\text{H}}$, become less important for increasing temperature. Notably, while H-abstractions by $\dot{\text{H}}$ contribute to the consumption of bulk carbon (red bars), generating active sites for further growth, H-abstractions by methyl radical ($\text{A-CH}_3 \text{ Abs}$) produce bulk carbon (blue bars), meaning that CH_4 in the gas phase is being consumed

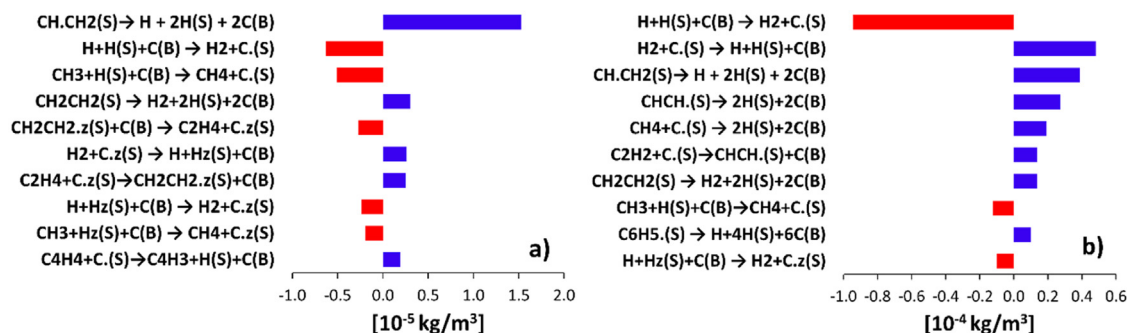


Fig. 11. Consumption (red) and production (blue) reactive fluxes [kg/m^3] of carbon bulk given by each elementary reaction. Figure a) shows the analysis at $T = 1173 \text{ K}$ and Figure b) at $T = 1323 \text{ K}$ ($A/V = 44 \text{ cm}^{-1}$, $P = 2.7 \text{ kPa}$, $\tau = 1 \text{ s}$, $t_R = 90 \text{ min}$).

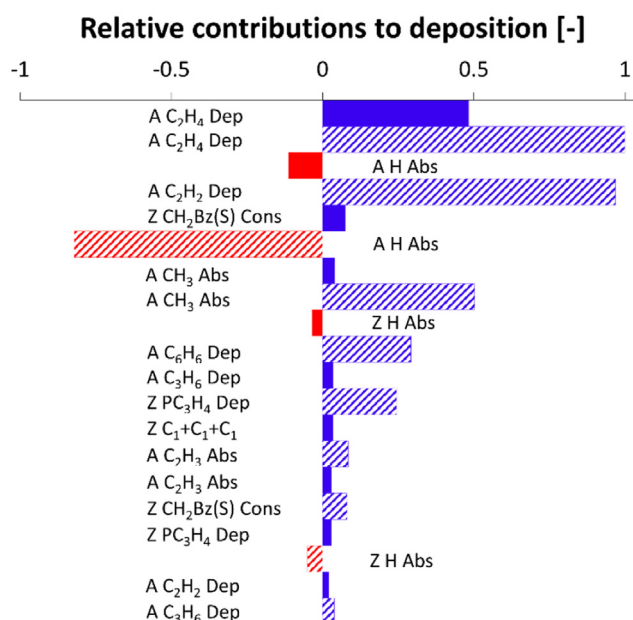


Fig. 12. Integral rate of production analysis on the most relevant reaction classes involved in the carbon deposition at 1173 K (full bars) and at 1323 K (weft bars) showing the sensitivity of our newly developed mechanism (PYR-SOOT) to temperature. ($A/V = 44 \text{ cm}^{-1}$, $P = 2.7 \text{ kPa}$, $\tau = 1 \text{ s}$, $t_R = 90 \text{ min}$).

by reactive armchair surface radicals. Other important reaction classes are propyne deposition on zigzag sites, propene deposition on armchair sites ($Z \text{ PC}_3\text{H}_4 \text{ Dep}/A \text{ C}_3\text{H}_6 \text{ Dep}$) and benzene deposition on armchair sites ($A \text{ C}_6\text{H}_6 \text{ Dep}$), the latter being much more relevant at higher temperatures. At the higher temperature, it is also relevant the sequential addition of three methyl ($Z \text{ C}_1 + \text{C}_1 + \text{C}_1$) on zigzag sites (Figure S8). It is also shown that, in the temperature range at which the flux analyses are performed (1173–1323 K), C_7H_7 is produced in low amounts and therefore its contribution to the deposit is negligible. Nevertheless, this reaction pathway would have a significant impact on the deposition rate at higher temperatures, in analogy with soot chemistry [17], therefore its introduction is legitimate for a comprehensive kinetic framework of general validity.

Fig. 13 presents cumulative contributions (%) of the different reaction classes to the formation of carbon bulk as a function of reaction time (t_R) in the surface PSR cases. By looking at the final time (namely at thermodynamic equilibrium), at lower temperatures the largest portion of deposit originates from ethylene deposition (~70%) on armchair sites. The remaining fraction comes from the deposition of acetylene (~10%), H-abstractions by methyl (CH_3) and vinyl (C_2H_3) radicals on armchair sites (~10%), propene deposition (<5%) and the successive addition of three methyl radicals (~10%) on zigzag sites (Figure S8). In addition, the pathway proceeding through $\text{CH}_2\text{Bz(S)}$ consumption ($Z \text{ CH}_2\text{Bz(S) Cons}$), which comes from the deposition of ethylene plus methyl ($\text{C}_2\text{H}_4 + \text{C}_1$ route), acetylene plus methyl ($\text{C}_2\text{H}_2 + \text{C}_1$ route) or propyne ($\text{C}_3\text{H}_4\text{-P}$) on zigzag sites (Figure S7) accounts for a significant proportion (~20%) of the deposited carbon in the lower temperature regime, however, it becomes irrelevant at higher temperatures.

What is more interesting is the dynamics at the very first instants (i.e., between 10^{-8} and 10^{-6} h) of the deposition process. Fig. 13 shows the predominance of CH_3 at lower temperature for the formation of solid carbon deposit. Specifically, CH_3 abstracts a hydrogen from the surface and deposits through the $\text{C}_1 + \text{C}_1 + \text{C}_1$ route on zigzag sites (Figure S8). After $\sim 10^{-6}$ h ethylene starts to form and its contribution to the deposit increases drastically through deposition on armchair sites until it reaches a maximum at around 10^{-3} h. This contribution decreases at

longer times favouring the deposition on zigzag sites. The preferential deposition on armchair sites may be explained by the fact that only one C_2 species (ethylene or acetylene), which are within the most abundant in the reacting mixture, is sufficient for creating a new aromatic ring on armchair sites, whereas the combination of C_2 and C_1 (CH_3) is required for the cyclization reactions on zigzag sites, being the concentration of C_3 (i.e., mainly $\text{C}_3\text{H}_4\text{-P}$) much lower. Therefore, the probability of having a successive deposition of C_2 and C_1 (or vice versa) must be smaller than the probability of direct deposition of one C_2 species. The high temperature ($T = 1323 \text{ K}$) analysis (Fig. 13b) shows how CH_3 formation is fostered by the increased thermal energy. While the qualitative behavior of C_2H_4 relative contribution is similar to the lower temperature case but shifted by one order of magnitude toward lower reaction times, its decrease after the peak is given by an increasingly important contribution of acetylene deposition on armchair sites. It can be also noticed that C_6H_6 deposition on armchair sites as well as propyne (PC_3H_4) deposition on zigzag sites start to contribute to the deposition process after around 10^{-5} h. Then, benzene deposition grows steadily until the end of the deposition process.

5.3. Hydrogen effect on carbon deposition from propane pyrolysis

The inhibiting effect of H_2 on carbon deposition from the pyrolysis of a propane/nitrogen mixture has been investigated from both an experimental and modeling perspective by I. Ziegler-Devin et al. [36]. Figure S18 of the SM compares measured and predicted profiles of gas phase species, including styrene, naphthalene and phenylacetylene showing significant improvements with respect to Lacroix et al. [9] model.

Fig. 14 compares experimental deposition rates as a function of H_2 mole fraction with predictions from both models. It stands out that the prediction with the model of Lacroix et al. [9] overestimates carbon deposition rate by ~30%, while the present model reproduces with high fidelity the experimental measurements both qualitatively and quantitatively. Overall, the present model better captures the inhibiting effect of H_2 on carbon deposition rates.

5.4. Effect of A/V ratio

Previous works [39–42], highlighted the important role of the ratio between the deposition surface area and the reactor volume (i.e., A/V) in pyrocarbon deposition processes. The validation of the newly developed model against some of these data is summarized in Sections S9 and S10 of the SM. First, a higher (or lower) ratio corresponds to a higher (or lower) contact time between gaseous species and the carbon deposit. A higher volume (i.e., lower A/V) increases the residence time of gaseous species. This aspect impacts the chemical nature of the depositing species and, as a result, alters the texture of the deposited carbon [41]. Figure S19 of the SM compares model results and the experimental data from Ziegler et al. [35] which reports a parametric analysis on A/V ratio of the most relevant gaseous species ($\text{C}_1\text{-C}_4$ and H_2).

Fig. 15 compares experimental deposition rates (a) and deposited mass (b) as a function of A/V ratio with model predictions. The updated model qualitatively and quantitatively agrees with the experimental measurements, predicting 30–50% lower amount of deposited mass compared to Lacroix et al. [9].

As reported in Fig. 16, the mass of carbon deposit monotonically increases as A/V increases, which is expected since the heterogeneous reactions pathway is promoted by a wider preform surface. By contrast, as C-atoms accumulate in the form of deposit, amorphous carbon mass in the gas phase decreases for larger A/V .

5.5. Methane pyrolysis in a plug flow reactor

Brüggert et al. [37] investigated pyrocarbon deposition from a 90% CH_4/Ar feedstock at $P = 100 \text{ kPa}$ and $T = 1323\text{--}1398 \text{ K}$ in a hot wall flow reactor. The reactor is a vertical ceramic tube which contains a

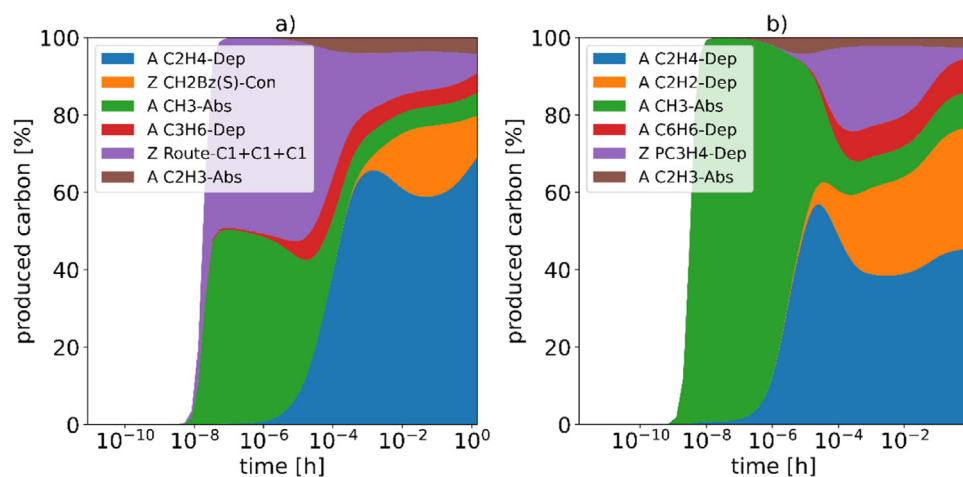


Fig. 13. Cumulative contributions (%) to the mass of carbon deposit divided by reaction class as a function of the reaction time (hours). Figure a) shows the analysis at 1173 K whereas b) at 1323 K.

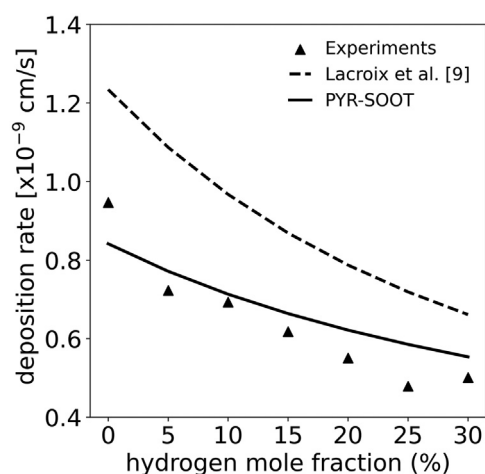


Fig. 14. Comparison of the models with experimental data [36] for the deposition rate for different hydrogen mole fractions at the inlet ($T = 1273$ K, $P = 2.7$ kPa, $A/V = 44$ cm $^{-1}$, $t_R = 90$ min, $\tau = 1$ s).

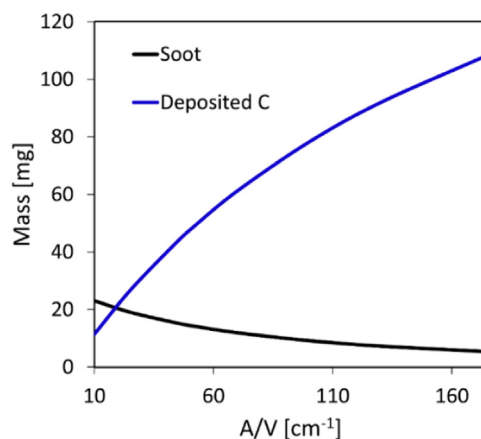


Fig. 16. Amorphous carbon mass (black line) and deposited carbon mass [mg] (blue line) as a function of the surface over volume ratio (A/V) ($T = 1273$ K, $P = 2.7$ kPa, $t_R = 90$ min, $\tau = 1$ s).

honeycomb structure made of cordierite to enhance the deposition surface. As reported in [37] this honeycomb structure contains 64 square shaped channels per cm 2 and each channel has a cross sectional area of 1.1 mm 2 . The residence time of the gaseous mixture inside the reactor is 1 s and the reactor length is 0.2 cm. Fig. 17 presents measured and sim-

ulated mole fraction profiles of the major gaseous species produced as a function of CH $_4$ conversion at $T = 1398$ K, confirming the capability of both models to correctly predict products selectivity. Model results for key gaseous compounds (e.g. H $_2$, CH $_4$, C $_2$ H $_4$, C $_2$ H $_2$, C $_6$ H $_6$) together with model predictions from Lacroix [9] as a function of residence time are also reported in Figure S26 of the SM.

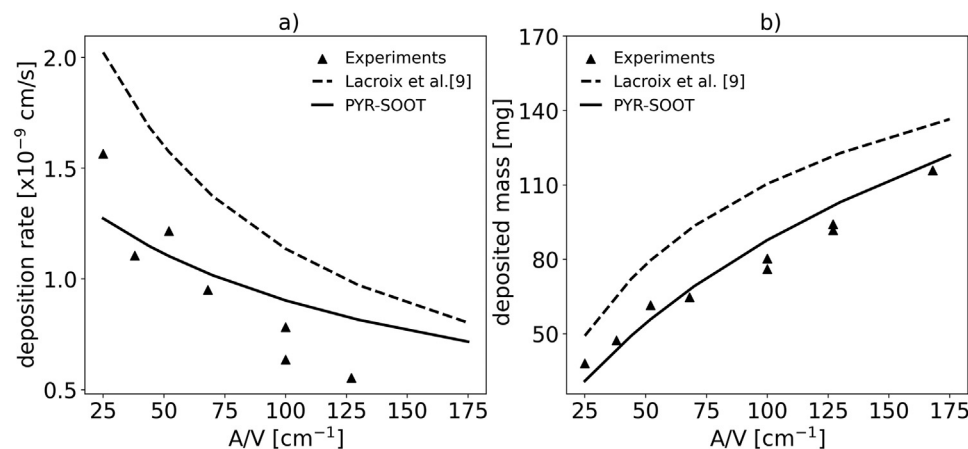


Fig. 15. Comparison of the models with experimental data [35] for the deposited mass at different surface over volume ratios. ($T = 1273$ K, $P = 2.7$ kPa, $t_R = 90$ min).

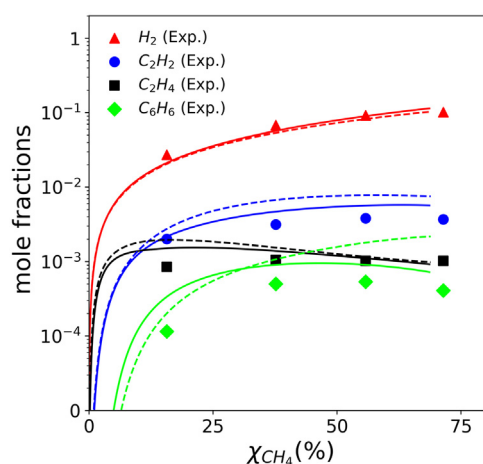


Fig. 17. Experimental (symbols) [37] and modelled yields of H_2 , C_2H_4 , C_2H_2 and C_6H_6 from 10% (mol/mol) CH_4 and 90% Ar pyrolysis at $T = 1323$ K and $P = 100$ kPa. The dashed lines: results from the model of Lacroix [9]. Continuous lines: results from the new model PYR-SOOT.

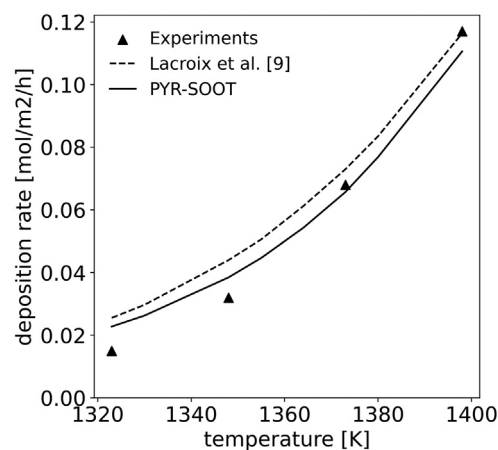


Fig. 18. Deposition rate as a function of reactor temperature ($\tau=1$ s, $P = 100$ kPa; $P_{CH_4}=10$ kPa). Comparison between experimental data [37] and simulations using Lacroix et al. [9] model (dashed line) and the present model with (solid line).

Fig. 18 compares measured pyrocarbon deposition rates [37] with model predictions. The results show that the present model is able to accurately predict the experimental deposition rates from [37] especially at high temperatures, where more amorphous carbon is formed. The model of Lacroix [9] overestimates by a factor of ~ 1.7 the deposition rate at low temperature while matching the experimental data at high temperature.

Results from a rate of production analysis performed on the heterogeneous PFR show the most relevant reaction classes which contribute to the mass of carbon deposit as a function of residence time (s) at 1323 K and 1398 K (Figure S27 of the SM). As in the case of propane pyrolysis, ethylene deposition on armchair sites plays a major role in the temperature range investigated (1323–1398 K). Propyne deposition on zigzag sites and $CH_2Bz(S)$ consumption account for more than 25% of the final deposited mass at 1323 K and around 45% at 1398 K. The deposition of acetylene and benzene become relevant at the higher temperature. Contrary to what was observed for propane deposition in the PSR, in this case propyne deposition on zigzag sites (*Z PC3H4 Dep*) has a higher contribution to deposition compared to acetylene.

6. Conclusions and perspectives

The detailed kinetic mechanism of pyrocarbon deposition from Lacroix et al. [9] has been updated in this work with rate constants of H-abstraction reactions obtained according to a systematic theoretical workflow based on state-of-the-art electronic structure calculations and transition state theory. Starting from the determination of rate constants of analogous reactions for gas phase model molecules with M062X density functional method, the existence of BEP correlations between energy barriers of activation and reaction enthalpies has been established for benzene and for PAHs with up to four aromatic rings. This latter investigation allowed to prove the size independence of the BEP correlation as well as providing the site-specific hindered rotor potentials of the different abstracting radicals, which have been applied as correction factors to the rate constants on zigzag and armchair sites. Then, the energy barriers of activation obtained for H-abstraction reactions by several abstracting radicals including those that are more relevant for pyrolysis conditions (e.g., H and CH_3) have been correlated with the energy barriers obtained in previous studies for H-abstraction reactions by the same radicals on armchair and zigzag graphene edges. Such correlations provide a straightforward approach to obtain energy barriers and thereof rate constants for heterogeneous processes by correcting the corresponding analogous gas phase reactions. The rate constants so determined are used to update the pyrocarbon deposition model from Lacroix et al. [9], coupled to a detailed gas phase kinetic subset including PAHs and amorphous carbon (soot) kinetics. The results obtained with this comprehensive kinetic framework have been validated by comparison with available literature data on the formation of solid carbon from the cracking of light hydrocarbons such as propane and methane. Our results suggest that accounting for the formation of amorphous carbon in the gas phase yields improved predictions of solid carbon deposited mass and deposition rate allowing to guide operating conditions optimization for the CVD/CVI process so as to minimize the loss of carbon in the form of soot. Rate of production and sensitivity analyses reveal the underlying dominant reaction pathways, highlighting margins for further refinement and improvement of model performances by extension of the proposed theoretical framework to other reaction classes of relevance (e.g. deposition of ethylene and acetylene on surface active sites) and by the inclusion of additional reaction pathways leading, for example, to defects in carbon texture. Overall, the present kinetic framework already allows for parametric investigation of carbon deposition processes for the production of “turquoise” hydrogen and carbon materials, thus enabling careful design of experiments and supporting reactor design.

Additional aspects to be improved in future upgrades of the present framework relate to the systematic inclusion of relevant reaction classes describing the interaction of MAH and PAHs with the solid surface. Specifically, beside abstractions of H atoms from the gas phase MAHs and PAHs by surface radicals together with their backward channels, deposition reactions of MAHs and PAHs molecules on active sites and the corresponding backward addition reaction of MAHs and PAHs radicals on the bulk carbon should be comprehensively accounted for and included.

In the perspective of industrial applications of this framework for processes such as the catalytic pyrolysis of hydrocarbons aimed at the co-production of H_2 and high added value carbon materials, it is of interest to also extend the surface model to embed the formation of structural defects in the solid carbon deposit. This includes for example the formation of pentagonal or heptagonal rings [39,41–43], which can be properly investigated by means of detailed kinetic models.

Declaration of Competing Interest

The authors declare that they have no known competing financial interests or personal relationships that could have appeared to influence the work reported in this paper.

Data availability

Data will be made available on request.

Acknowledgements

The authors acknowledge financial support from the Italian Ministry of University and Research (MIUR), from Brembo S.p.A. and from the Carbon Hub (<https://carbonhub.rice.edu/>).

Supplementary materials

Supplementary material associated with this article can be found, in the online version, at [doi:10.1016/j.cartre.2023.100263](https://doi.org/10.1016/j.cartre.2023.100263).

References

- Jad Diab, et al., Why turquoise hydrogen will be a game changer for the energy transition, *Int. J. Hydrogen Energy* (2022).
- M. Hermesmann, T.E. Müller, Green, turquoise, blue, or grey? Environmentally friendly hydrogen production in transforming energy systems, *Prog. Energy Combust. Sci.* 90 (2022) 100996.
- N. Sánchez-Bastardo, R. Schlögl, H. Ruland, Methane pyrolysis for CO₂-free H₂ production: a green process to overcome renewable energies unsteadiness, *Chem. Ing. Tech.* 92 (2020), doi:10.1002/cite.202000029.
- , Opinion: we can use carbon to decarbonize—and get hydrogen for free” Matteo Pasquali, Carl Mesters, in: *Proceedings of the National Academy of Sciences*, 118, Aug 2021, doi:10.1073/pnas.2112089118.
- G. Bozzano, et al., Fouling phenomena in pyrolysis and combustion processes, *Appl. Therm. Eng.* 22 (8) (2002) 919–927.
- S. Wauters, G.B. Marin, Kinetic modeling of coke formation during steam cracking, *Ind. Eng. Chem. Res.* 41 (10) (2002) 2379–2391.
- G.M. Jenkins, C.J. Grigson, The fabrication of artifacts out of glassy carbon and carbon-fiber-reinforced carbon for biomedical applications, *J. Biomed. Mater. Res.* 13 (1979) 371–394, doi:10.1002/jbm.820130304.
- Gerard L. Vignoles, Francis Langlais, Cédric Descamps, Arnaud Mouchon, Hélène Le Poche, Nicolas Reuge, Nathalie Bertrand, CVD and CVI of pyrocarbon from various precursors, *Surf. Coat. Technol.* 188–189 (2004) 241–249. VolumePages, doi:10.1016/j.surfcoat.2004.08.036.
- R. Lacroix, R. Fournet, I. Ziegler-Devin, P.-M. Marquaire, Kinetic modeling of surface reactions involved in CVI of pyrocarbon obtained by propane pyrolysis, *Carbon* 48 (1) (2010) 132–144. VolumeIssuePagesISSN 0008-6223, doi:10.1016/j.carbon.2009.08.041.
- M. Frenklach, H. Wang, Detailed surface and gas-phase chemical kinetics of diamond deposition, *Phys. Rev. B* 43 (1991) 1520–1545.
- Özlem Yönder, et al., Can small polyaromatics describe their larger counterparts for local reactions? A computational study on the H-abstraction reaction by an H-atom from polyaromatics, *J. Phys. Chem. A* 124 (46) (2020) 9626–9637.
- Zhao-Bin Ding, et al., First-principles assessment of the analogy between gas-phase and gas-solid H-abstraction reactions at graphene edges, *Chem. Eng. J.* 377 (2019) 119691.
- Ghobad Bagheri, et al., Comprehensive kinetic study of combustion technologies for low environmental impact: MILD and OXY-fuel combustion of methane, *Combust. Flame* 212 (2020) 142–155.
- Eliseo Ranzi, et al., Reduced kinetic schemes of complex reaction systems: fossil and biomass-derived transportation fuels, *Int. J. Chem. Kinet.* 46 (9) (2014) 512–542.
- Ranzi, et al., Hierarchical and comparative kinetic modeling of laminar flame speeds of hydrocarbon and oxygenated fuels, *Prog. Energy Combust. Sci.* 38 (4) (2012) 468–501.
- Warumporn Pejpichestakul, et al., Examination of a soot model in premixed laminar flames at fuel-rich conditions, *Proc. Combust. Inst.* 37 (1) (2019) 1013–1021.
- Andrea Nobili, et al., On the radical behavior of large polycyclic aromatic hydrocarbons in soot formation and oxidation, *Combust. Flame* 235 (2022) 111692.
- Andrea Nobili, et al., Modeling soot particles as stable radicals: a chemical kinetic study on formation and oxidation. Part I. Soot formation in ethylene laminar premixed and counterflow diffusion flames, *Combust. Flame* (2022) 112073.
- Y. Zhao, D.G. Truhlar, The M06 suite of density functionals for main group thermochemistry, thermochemical kinetics, noncovalent interactions, excited states, and transition elements: two new functionals and systematic testing of four M06-class functionals and 12 other functionals, *Theor. Chem. Acc.* 120 (2008) 215–241, doi:10.1007/s00214-007-0310-x.
- Daniela Josa, Jesús Rodríguez-Otero, Enrique M. Cabaleiro-Lago, Marcos Relán-Piñeiro, Analysis of the performance of DFT-D, M05-2X and M06-2X functionals for studying π – π interactions, *Chem. Phys. Lett.* 557 (2013) 170–175. VolumePage-sISSN 0009-2614.
- J.A. Montgomery Jr., M.J. Frisch, J.W. Ochterski, G.A. Petersson, A complete basis set model chemistry. VI. Use of density functional geometries and frequencies, *J. Chem. Phys.* 110 (1999) 2822–2827, doi:10.1063/1.477924.
- J.W. Ochterski, G.A. Petersson, J.A. Montgomery Jr., A complete basis set model chemistry. V. Extensions to six or more heavy atoms, *J. Chem. Phys.* 104 (1996) 2598–2619, doi:10.1063/1.470985.
- Active thermochemical tables: thermochemistry for the 21st by Branko Ruscic, A Reinhardt E. Pinzon, A Gregor Von Laszewski, Deepti Kodeboyina, B. Alex, Er Burcat, C David Leahy, David Montoya, Albert F. Wagner A, 2005.
- C. Cavallotti, M. Pelucchi, Y. Georgievskii, S.J. Klippenstein, EStokTP: electronic structure to temperature-and pressure-dependent rate constants-a code for automatically predicting the thermal kinetics of reactions, *J. Chem. Theory Comput.* 15 (2019) 1122–1145.
- B.R. Giri, T. Bentz, H. Hippler, M. Olzmann, Shock-tube study of the reactions of hydrogen atoms with benzene and phenyl radicals, *Zeitschrift Fur Phys. Chemie* 223 (2009) 539–549.
- T.V.T. Mai, A. Ratkiewicz, M.V. Duong, L.K. Huynh, Direct ab initio study of the C₆H₆ + CH₃/C₂H₅ = C₆H₅ + CH₄/C₂H₆ reactions, *Chem. Phys. Lett.* 646 (2016) 102–109.
- M. Krech and S.J.W. Price. Hydrogen abstraction by methyl radicals from benzene and the pressure dependence of the recombination of methyl radicals. *Can. J. Chem.* 45(2): 157–159.
- H.-X. Zhang, S.I. Ahonkhah, M.H. Back, Rate constants for abstraction of hydrogen from benzene, toluene, and cyclopentane by methyl and ethyl radicals over the temperature range 650–770K, *Can. J. Chem.* 67 (1989) 1541–1549.
- M.G. Evans, M. Polanyi, Inertia and driving force of chemical reactions, *Trans. Faraday Soc.* 34 (1938) 11–24.
- Stephen J. Klippenstein, Carlo Cavallotti, Ab initio kinetics for pyrolysis and combustion systems, *Comput. Aided Chem. Eng.* 45 (2019) 115–167 Elsevier.
- T. Bieleveld, A. Frassoldati, A. Cuoci, T. Faravelli, E. Ranzi, U. Niemann, K. Seshadri, Experimental and kinetic modeling study of combustion of gasoline, its surrogates and components in laminar non-premixed flows, in: *Proceedings of the Combustion Institute* 32 I, 2009, pp. 493–500, doi:10.1016/j.proci.2008.06.214.
- C. Saggese, Cuoci A. Frassoldati, Faravelli T. Ranzi, A wide range kinetic modeling study of pyrolysis and oxidation of benzene, *Combust. Flame* (2013), doi:10.1016/j.combustflame.2013.02.013.
- E. Ranzi, T. Faravelli, P. Gaffuri, E. Garavaglia, A. Goldaniga, Primary pyrolysis and oxidation reactions of linear and branched alkanes, *Ind. Eng. Chem. Res.* 36 (8) (1997) 3336–3344.
- I. Ziegler, R. Fournet, P.M. Marquaire, Pyrolysis of propane for CVI of pyrocarbon: part II. Experimental and modeling study of polyaromatic species, *J. Anal. Appl. Pyrolysis* 73 (2) (2005) 231–247.
- I. Ziegler, R. Fournet, P.M. Marquaire, Pyrolysis of propane for CVI of pyrocarbon: part I. Influence of surface on chemical kinetic of pyrocarbon deposition obtained by propane pyrolysis, *J. Anal. Appl. Pyrolysis* 73 (2005) 107–115.
- I. Ziegler-Devin, R. Fournet, R. Lacroix, P.M. Marquaire, An interpretation of the hydrogen inhibiting effect on chemical vapor deposition of pyrocarbon, *J. Anal. Appl. Pyrolysis* 115 (2015) 299–306.
- M. Brüggert, Z. Hu, K.J. Hüttinger, Chemistry and kinetics of chemical vapor deposition of pyrocarbon: VI. Influence of temperature using methane as a carbon source, *Carbon* 37 (1999) 2021–2030.
- Alberto Cuoci, Alessio Frassoldati, T. Faravelli, Eliseo Ranzi, OpenSMOKE++: an object-oriented framework for the numerical modeling of reactive systems with detailed kinetic mechanisms, *Comput. Phys. Commun.* (2015) In press, doi:10.1016/j.cpc.2015.02.014.
- W.G. Zhang, K.J. Hüttinger, Chemical vapor deposition of carbon from methane at various pressures, partial pressures and substrate area/reactor volume ratios, *J. Mater. Sci.* 36 (14) (2001) 3503–3510.
- A. Becker, K.J. Hüttinger, Chemistry and kinetics of chemical vapour deposition of pyrocarbon-IV pyrocarbon deposition from methane in the low-temperature regime, *Carbon* 36 (1998) 213–224.
- Z. Hu, K.J. Hüttinger, Chemistry and kinetics of chemical vapor deposition of pyrocarbon—VIII. Carbon deposition from methane at low pressures, *Carbon* 39 (3) (2001) 433–441.
- K.J. Hüttinger, CVD in hot wall reactors—the interaction between homogeneous gas-phase and heterogeneous surface reactions, *Adv. Mater.—CVD* 4 (4) (1998) 151–158.
- G.L. Dong, K.J. Hüttinger, Consideration of reaction mechanisms leading to pyrolytic carbon of different textures, *Carbon* 40 (14) (2002) 2515–2528. VolumeIssuePage-sISSN 0008-6223, doi:10.1016/S0008-6223(02)00174-4.